AIAA 82-4241

Pneumatic Tire Model for Aircraft Simulation

J. R. Kilner*
Boeing Military Airplane Company, Seattle, Washington

The development of a tire model for the prediction of vertical and drag loads in response to large discrete surface obstacles shorter than the tire footprint length is presented. The tire is modeled as a toroidal membrane with the objective of characterizing the enveloping properties of the tire. An explicit set of equations is used to calculate the tire footprint in contact with a user specified surface profile, the tire volume, the pneumatic pressure, and the resultant vertical and drag loads at the wheel axle. Tire carcass and bottoming loads are also predicted. The model is designed to be computationally efficient for use with aircraft digital taxi simulations. Model predictions are compared with tire test data for low-speed fixed axle excursions over short rectangular bumps and dips. Excellent quantitative correlation is demonstrated.

Nomenclature

A_u, A_v = horizontal and vertical projections of the tire footprint area
A_s = tire section area
b = vertical intercept in the wheel coordinate system
B = tire section height
B_t = tire deflection at bottoming threshold
C_b = tire bottoming constant
C_V = tire volume constant
F_u, F_v = total drag and vertical tire loads
F_b = total tire bottoming load
F_{bu}, F_{bv} = drag and vertical tire bottoming loads
L_c = tire carcass load
m = surface profile slope
n = number of points defining surface profile
P = effective pneumatic pressure (gage)
P_a = ambient pressure
P_c = carcass pressure shift
P_p = tire pneumatic pressure (gage)
P_0 = tire inflation pressure (gage)
R = radial distance from the wheel axle
R_0 = tire outside radius
R_b = radial tire bottoming threshold
s = surface length
u, v = wheel coordinates
$\tilde{u}_1, \tilde{u}_2$ = left and right limits of each section for pneumatic loads
$\hat{u}_1, \hat{u}_2$ = left and right limits of each section for bottoming loads
V' = lost tire volume
V_t = volume of the undeflected tire
W = footprint width
W_t = section width of the undeflected tire
x_i, z_i = series of points in the Earth coordinate system (position and elevation) defining the surface profile
x_s, z_s = axle position and elevation in the Earth coordinate system
y = position of the tire section centroid relative to the undeflected tire periphery
δ = tire deflection
θ = slope of the surface profile
ϕ = angular position in the wheel coordinate system
Ω = tire volume function

Subscripts

k = variables associated with the individual tire sections
m = variables at the midpoint of the bottomed section element $\hat{u}_1, \hat{u}_2$
0 = undeflected state

Received August 26, 1981.

*Lead Engineer, Landing Gear Systems.

Introduction

A COMPUTATIONALLY efficient tire model is required for time-history digital simulations designed to predict aircraft dynamics in response to runway surface roughness. These simulations typically contain 20-40 nonlinear state equations, as well as numerous algebraic and trigonometric equations, that model the dynamic behavior of the rigid and elastic airframe, the aerodynamic loads, nose and main gear shock strut loads, unsprung mass dynamics, and the tire/ground reactions. To be compatible with other component models that make up the overall simulation, the tire model must consist of an explicit set of equations that predicts the tire vertical and drag ground reactions applied at the wheel axle as a function of axle position relative to a defined surface elevation profile. The standard technique is to use a point contact spring model based on tire load-deflection test data.[1,2] The vertical load is predicted by the test data and the drag load is calculated as the product of the vertical load and the surface slope under the axle. The spring model is a valid technique for long-wavelength (>10-ft) gradual-slope (<5%) surface irregularities. However, for surface irregularities less than 10 ft long the model predictions begin to deviate from corresponding test data. The problem is particularly severe for discrete surface irregularities that are shorter than the tire footprint length such as step bumps, surface spalls (chuck holes), and barrier cables. In this case the spring model will produce gross errors in its load predictions since the model contacts the ground at a point and follows the exact contour of the surface, producing a proportional load profile. However, an actual tire passing over the same surface irregularity will produce much less load variation due to the characteristic of the pneumatic tire to partially or wholly envelop (or swallow) these discrete surface irregularities.

A number of distributed contact tire models have been proposed, such as multiple parallel or radial spring arrangements in contact with the ground,[2] elastically supported cylindrical shell representing tire carcass and pneumatic characteristics,[3] and linear superposition techniques based on measured tire response to step inputs.[4] However, these models have limitations which preclude their use for aircraft taxi simulation. These limitations include requirements for special tire testing to acquire model input

data; computational inefficiency as a result of extremely complex model equations; the lack of wheel hop and wheel bottoming capability; and the inability to accommodate large obstacles.

Pneumatic Tire Model Description

The author has developed a tire model that overcomes the limitations of the spring-type models by representing, in equation form, the physical function of a pneumatic tire in contact with an irregular surface. The model calculates the vertical and drag loads at the wheel axle based on the relative position of the axle to a user-defined surface elevation profile. This is accomplished by determining the footprint area of the tire (represented as a toroidal membrane) in contact with the defined surface, the change in tire volume, and the resulting change in pneumatic pressure. The tire vertical and drag loads are then the product of the pneumatic pressure and the vertical and horizontal projections of footprint area (Fig. 1). Other features of the model follow:

1) The model will determine loads for tire interaction with any user specified piecewise linear surface elevation profile. The surface is assumed rigid.

2) The model can encounter abrupt surface elevation variations (such as step bumps) up to the wheel axle level.

3) The model will calculate vertical and drag tire bottoming loads when the tire tread inner surface contacts side-wall rubber near the tire bead.

4) The model includes the static load carrying characteristic of the tire carcass.

5) The model requires only seven input parameters (to characterize a given tire) which can be extracted from tire load-deflection data sheets readily available from the tire manufacturer.

6) The model equations are explicitly evaluated (i.e., no iteration required) resulting in a computationally efficient algorithm compatible with aircraft digital taxi simulation.

Also, it is assumed that the rolling tire does not slip and tire damping and hysteresis effects are negligible compared to other system damping present in the overall aircraft simulation.

Development of Governing Equations

The fundamental principle of the model is that the vertical and horizontal tire reactions,

$$F_v = PA_v + F_{bv} \tag{1}$$

$$F_u = PA_u + F_{bu} \tag{2}$$

are the product of the vertical and horizontal projections of the tire footprint and the tire pneumatic pressure (Fig. 1), plus the respective components of tire bottoming load. The tire pneumatic pressure is a function of the lost tire volume V' due to tire deflection. Tire loads F_v and F_u are calculated for a given wheel axle position x_s and z_s, in the Earth coordinate system, relative to a surface profile represented as a piecewise linear function. This function is defined by the series of points

$$(x_1,z_1),(x_2,z_2),\ldots,(x_n,z_n)$$

where the elevation for x outside of the series is defined by the nearest z_i. The number of points for typical surface irregularities are $n=2$ for a step bump and $n=8$ for a pair of surface spalls.

To simplify the calculations the footprint areas, tire volume and bottoming loads are evaluated for each tire section ($k=1,2,\ldots$) as shown in Fig. 2. The sections are defined by the endpoints of each surface element (such as c and d) and/or the intersection of the tire circumference (assumed constant) and the surface profile element (such as b and e). These sections are assumed to act independently of one another. Thus the total tire areas, lost volume, and bottoming loads are

$$A_v = \sum_k A_{vk} \tag{3a}$$

$$A_u = \sum_k A_{uk} \tag{3b}$$

$$V'/V_t = \sum_k V'_k/V_t \tag{3c}$$

$$F_{bv} = \sum_k F_{bvk} \tag{3d}$$

$$F_{bu} = \sum_k F_{buk} \tag{3e}$$

The subscript k for tire section variables, other than those used in Eqs. (3a-3e), will hereafter be dropped for clarity.

Tire Footprint Area

The footprint area equations are derived using the differential footprint area element in the kth tire section shown in Fig. 3. The vertical and horizontal projections are

$$dA_{vk} = w\cos\theta ds = w du$$

$$dA_{uk} = w\sin\theta ds = wm du$$

where

$$m = \tan\theta = \frac{(z_{i+1}-z_i)}{(x_{i+1}-x_i)} \tag{4}$$

It is assumed that the differential element ds of the pneumatic tire can be reasonably idealized as an independent

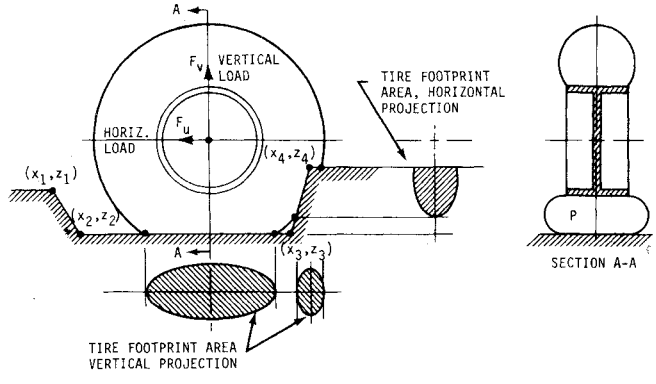

Fig. 1 Toroidal membrane tire model.

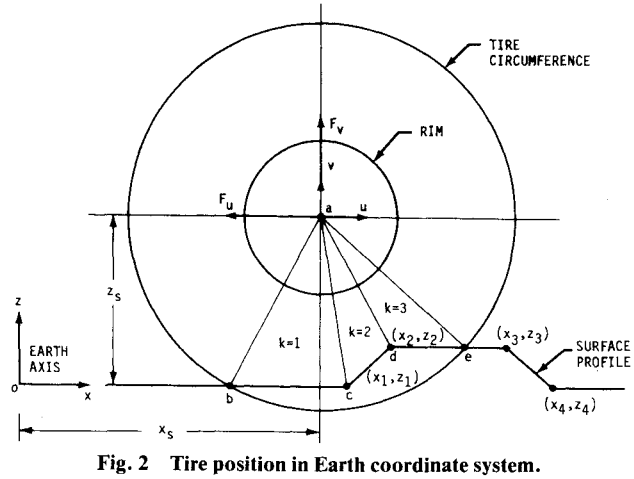

Fig. 2 Tire position in Earth coordinate system.

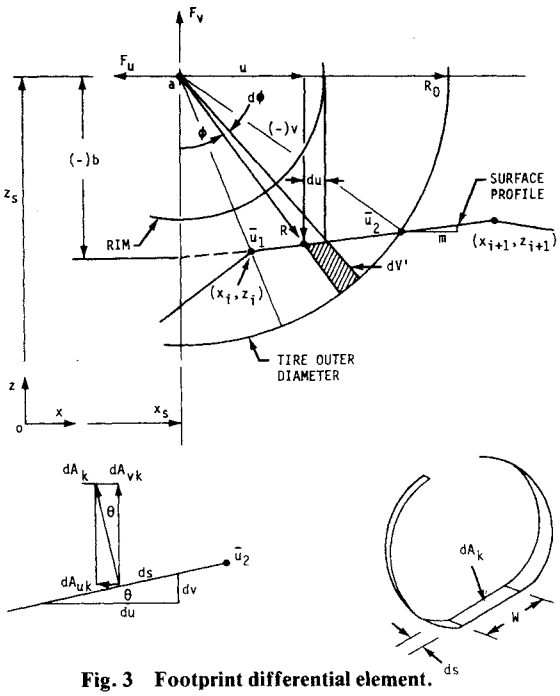

Fig. 3 Footprint differential element.

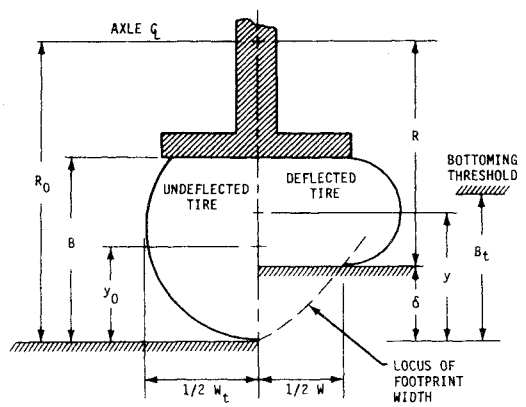

Fig. 4 Inelastic membrane representation of the tire section.

two-dimensional inelastic membrane as shown in Fig. 4. Therefore the footprint width W becomes a function of R alone. The area projections of the tire section $a\bar{u}_1\bar{u}_2$ are then

$$A_{vk} = \int_{\bar{u}_1}^{\bar{u}_2} W(R)\,du \tag{5}$$

$$A_{uk} = mA_{vk} \tag{6}$$

where

$$R = (u^2+v^2)^{1/2} = [u^2+(mu+b)^2]^{1/2} \tag{7}$$

$$v = mu+b \tag{8}$$

$$b = (z_i - z_s) - m(x_i - x_s) \tag{9}$$

In nondimensional form the membrane footprint width is an implicit function of tire deflection, $\delta/W_t = (R_0-R)/W_t$, and tire aspect ratio B/W_t requiring an iterative solution of three trigonometric equations. This relationship is shown in Fig. 5 for $B/W_t = 0.9$ and 0.8, which is the range for type VII aircraft tires. These curves are compared to type VII tire test data[5] to indicate the degree of mathematical idealization. However, an iterative solution of the membrane equations is inconsistent with the objective of achieving a computationally

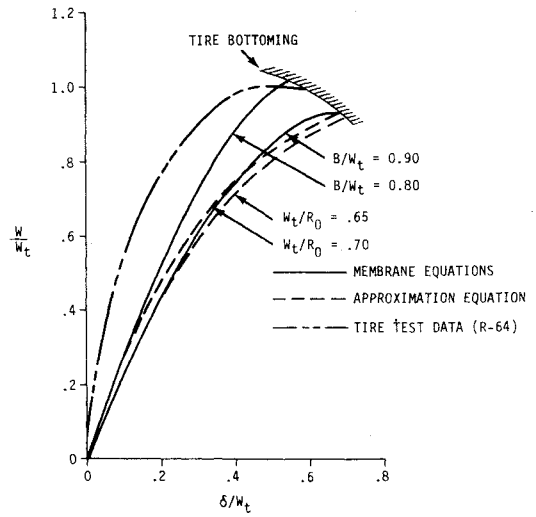

Fig. 5 Nondimensional footprint width vs tire deflection.

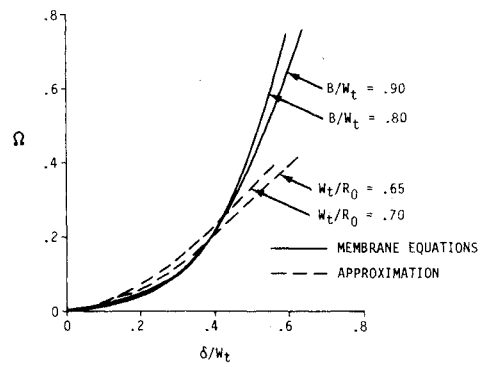

Fig. 6 Tire volume function vs nondimensional tire deflection.

efficient tire model. Also, an integrable function is required which precludes the use of test data directly. To avoid these limitations the function W/W_t is adequately approximated by

$$\frac{W}{W_t} = 1-\left(\frac{R}{R_0}\right)^4 = 1-\left(1-\frac{W_t}{R_0}\frac{\delta}{W_t}\right)^4 \tag{10}$$

Equation (10) is shown in Fig. 5 for values of $W_t/R_0 = 0.7$ and 0.65, which are comparable to values of $B/W_t = 0.8$ and 0.9, respectively, for type VII tires. Substituting Eqs. (7) and (10) into Eq. (5), and evaluating the integral yields

$$A_{vk} = W_t\left\{(\bar{u}_2-\bar{u}_1) - \frac{1}{R_0^4}\left[\frac{1}{5}(1+m^2)^2(\bar{u}_2^5-\bar{u}_1^5) + (1+m^2)mb(\bar{u}_2^4-\bar{u}_1^4) + \frac{2}{3}(1+3m^2)b^2(\bar{u}_2^3-\bar{u}_1^3) + 2mb^3(\bar{u}_2^2-\bar{u}_1^2) + b^4(\bar{u}_2-\bar{u}_1)\right]\right\} \tag{11}$$

Tire Pneumatic Pressure and Volume

The tire pneumatic pressure P_p is assumed to be a reversible adiabatic process expressed by

$$P_p = (P_0+P_a)\left(\frac{1}{1-V'/V_t}\right)^{1.4} - P_a \tag{12}$$

where V' is the total tire volume lost owing to tire deflection. The undeflected tire volume is approximated by

$$V_t = 2\pi(R_0 - \tfrac{1}{2}B_t)A_{s0} \tag{13}$$

where A_{s0} is the undeflected tire cross-sectional area and the quantity $(R_0 - \frac{1}{2}B_t)$ is the approximate radial distance from the wheel axle to the area centroid (Fig. 4). The lost tire volume V'_k for the differential element shown in Fig. 3 and tire dimensions shown in Fig. 4 is

$$dV'_k = A_{s0}(R_0 - y_0)\,d\phi - A_s(R_0 - y)\,d\phi$$

Noting that

$$d\phi = -(v/R^2)\,du$$

the lost volume is

$$V'_k = \frac{A_{s0}}{R_0}\int_{\bar{u}_1}^{\bar{u}_2} v\Omega\,du \tag{14}$$

where

$$\Omega = \left(\frac{R_0}{R}\right)^2\left[\left(1 - \frac{y_0}{R_0}\right) - \frac{A_s}{A_{s0}}\left(1 - \frac{y}{R_0}\right)\right] \tag{15}$$

Equation (15) is evaluated from the implicit membrane equations and is shown in Fig. 6 for the range of aspect ratios B/W_t typical of type VII tires. Following the approach established for the footprint area, Ω is approximated with the explicit function

$$\Omega = C_V\left[1 - \left(\frac{R}{R_0}\right)^2\right]^2 = C_V\left[1 - \left(1 - \frac{W_t}{R_0}\frac{\delta}{W_t}\right)^2\right]^2 \tag{16}$$

where C_V is a constant associated with the tire volume. This equation is compared with the membrane equations in Fig. 6 for a corresponding range of W_t/R_0 typical of type VII tires. The constant C_V is unity for the comparison. Using this approximation, the lost internal volume for the kth section (Fig. 3) can then be evaluated from Eqs. (7), (8), (13), (14), and (16), which yields

$$\begin{aligned}\frac{V'_k}{V_t} = \frac{-C_V}{2\pi R_0^5(R_0 - \frac{1}{2}B_t)}\Big\{&\frac{1}{6}m(1+m^2)^2(\bar{u}_2^6 - \bar{u}_1^6)\\ &+\frac{1}{5}b(1+m^2)(1+5m^2)(\bar{u}_2^5 - \bar{u}_1^5)\\ &+\tfrac{1}{2}m[2m^2b^2 - (1+m^2)(R_0^2 - 3b^2)](\bar{u}_2^4 - \bar{u}_1^4)\\ &+\frac{2}{3}b[2m^2b^2 - (1+3m^2)(R_0^2 - b^2)](\bar{u}_2^3 - \bar{u}_1^3)\\ &+\frac{1}{2}m(R_0^2 - b^2)(R_0^2 - 5b^2)(\bar{u}_2^2 - \bar{u}_1^2)\\ &+b(R_0^2 - b^2)^2(\bar{u}_2 - \bar{u}_1)\Big\}\end{aligned} \tag{17}$$

The tire volume constant C_V is evaluated based on aircraft tire parametric and test data relating the undeflected-to-bottomed pressure ratio and nondimensional bottomed deflection B_t/R_0 for 11 type VII tires shown in Fig. 7. This relationship is approximated by

$$\left(\frac{P_p + P_a}{P_0 + P_a}\right)_{\delta = B_t} = \left(1 + \frac{3}{8}\frac{B_t}{R_0}\right)^{1.4} \tag{18}$$

Substituting Eq. (18) into Eq. (12) and solving for V'/V_t yields

$$\left(\frac{V'}{V_t}\right)_{\delta = B_t} = \frac{3}{8}\frac{B_t}{R_0}\Big/\left(1 + \frac{3}{8}\frac{B_t}{R_0}\right) \tag{19}$$

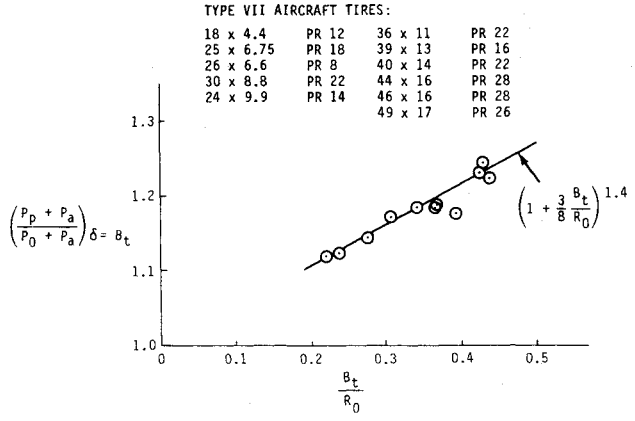

Fig. 7 Relationship between bottomed tire pneumatic pressure and deflection.

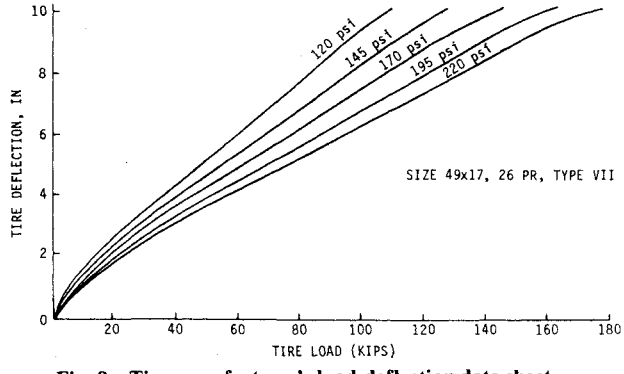

Fig. 8 Tire manufacturer's load-deflection data sheet.

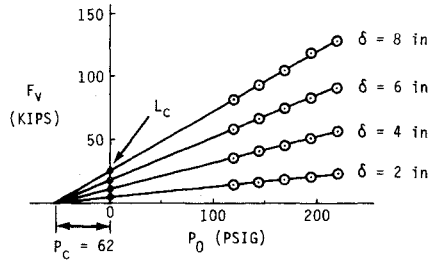

Fig. 9 Static load carrying characteristic of the tire carcass.

Equating Eqs. (17) and (19), noting that for a bottomed tire on a flat surface

$$m = 0$$

$$b = -(R_0 - B_t)$$

$$\bar{u}_2 = -\bar{u}_1 = (2R_0B_t - B_t^2)^{1/2} \tag{20}$$

results in

$$C_V = \frac{1.1045(B_t/R_0)(2 - B_t/R_0)}{(1 + \frac{3}{8}B_t/R_0)(1 - B_t/R_0)[2B_t/R_0 - (B_t/R_0)^2]^{5/2}} \tag{21}$$

Tire Carcass Pressure Constant

The static load carrying capability of the tire carcass is approximated in the pneumatic tire model by adding a

constant term to Eq. (12) so that

$$P=P_p+P_c=(P_0+P_a)\left(\frac{1}{1-V'/V_t}\right)^{1.4}-P_a+P_c \quad (22)$$

where P_c is called the carcass pressure shift and P is then the effective pneumatic pressure. The existence of P_c is demonstrated by plotting and interpreting tire test data. This is shown by first modifying Eq. (1) to include a carcass load term L_c which is assumed to be a function of tire deflection alone, so that

$$F_v=P_p(\delta,P_0)A_v(\delta)+F_{bv}+L_c(\delta) \quad (23)$$

The tire carcass load can then be determined from static tire load-deflection data like that shown in Fig. 8. Replotting load F_v vs inflation pressure P_0 for a family of constant tire deflection curves (Fig. 9) yields the carcass load L_c, since $F_v \approx L_c(\delta)$ when $P_p(\delta,0)\approx 0$ for all δ, and $F_{bv}=0$ for $\delta<B_t$.

Substituting Eq. (22) into Eq. (1) and equating to Eq. (23) for $\delta<B_t$, so that

$$F_v=(P_p+P_c)A_v=P_pA_v+L_c \quad (24)$$

yields

$$P_c=L_c/A_v \quad (25)$$

The validity of Eq. (25) is supported by calculating the ratio L_c/A_v using Eq. (23) for several values of δ and P_0. The results are shown in Fig. 10. Values for tire load F_v were selected from Fig. 8, and A_v and P_p were calculated using Eqs. (11), (12), and (17).

Tire Bottoming Load

When highly loaded, the inner surface of the tire tread eventually makes contact with the tire structure near the bead. This happens when $\delta=B_t$ and is called tire bottoming. When contact occurs a significant portion of the load is transmitted through the carcass structure.

Modeling this phenomenon is essential to perform aircraft time-history simulation since tire bottoming does occur. However, the carcass and the rubber-to-rubber contact zone are very complex structures, and thus difficult to describe mathematically. Since bottoming occurs occasionally during vehicle simulation, and then very briefly, a much simpler approach is taken to characterize tire bottoming load, thereby avoiding a detailed analysis of the elastic structure.

It is assumed that the wheel axle load resulting from tire bottoming is proportional to the volume of rubber displaced as shown in Fig. 11. Therefore the load for the tire section

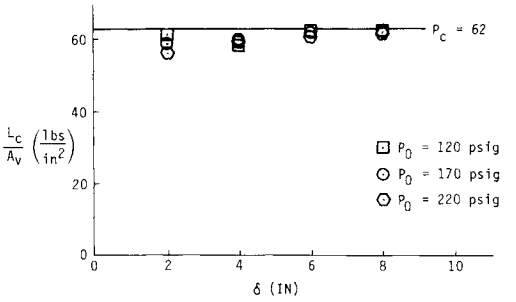

Fig. 10 Ratio of carcass load to footprint area for a given carcass pressure shift.

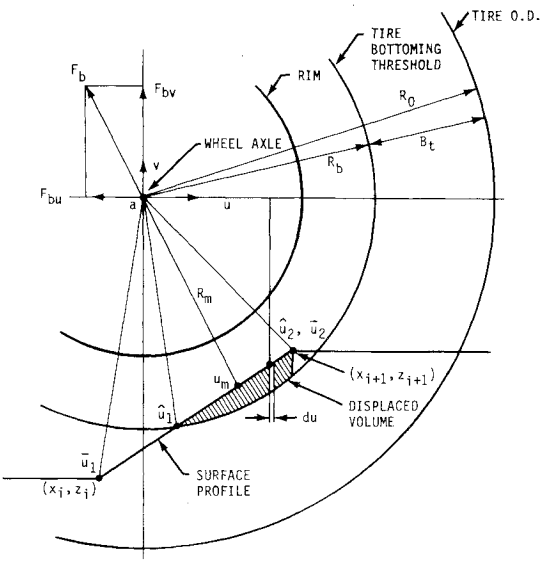

Fig. 11 Model of displaced rubber during tire bottoming.

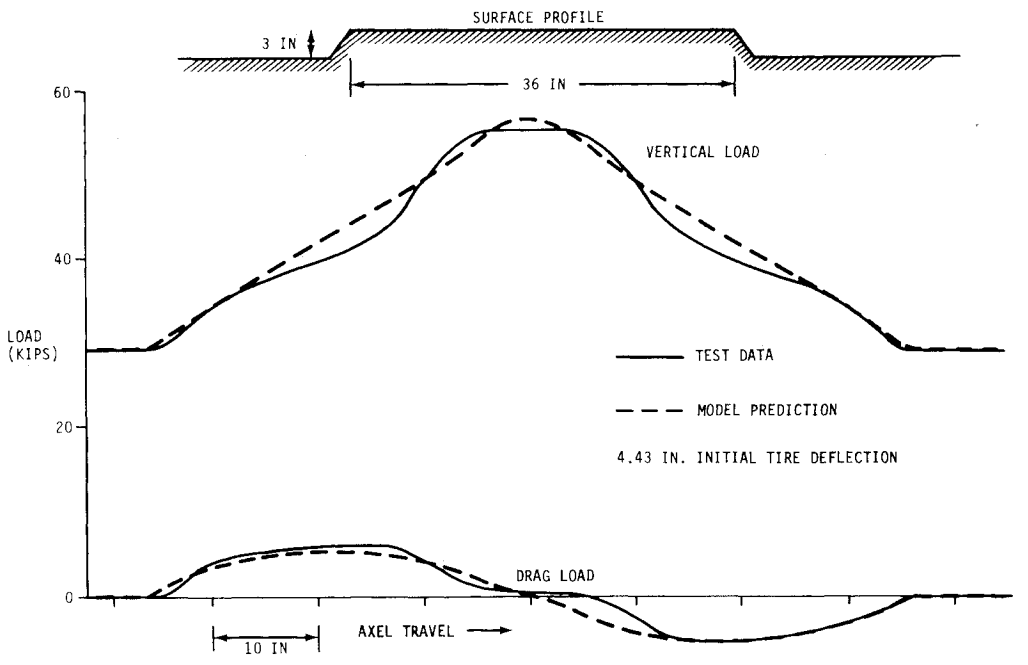

Fig. 12 Fixed axle excursion over 36×3-in. bump.

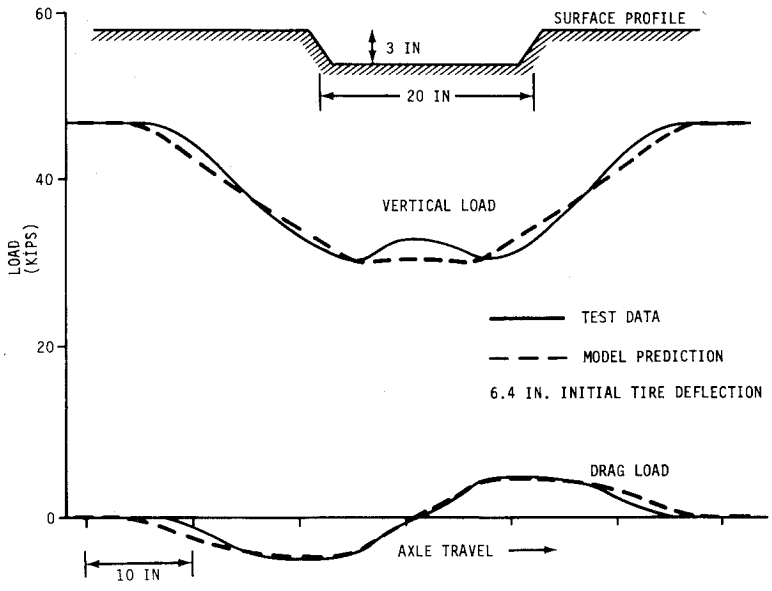

Fig. 13 Fixed axle excursion over 20 × 3-in. dip.

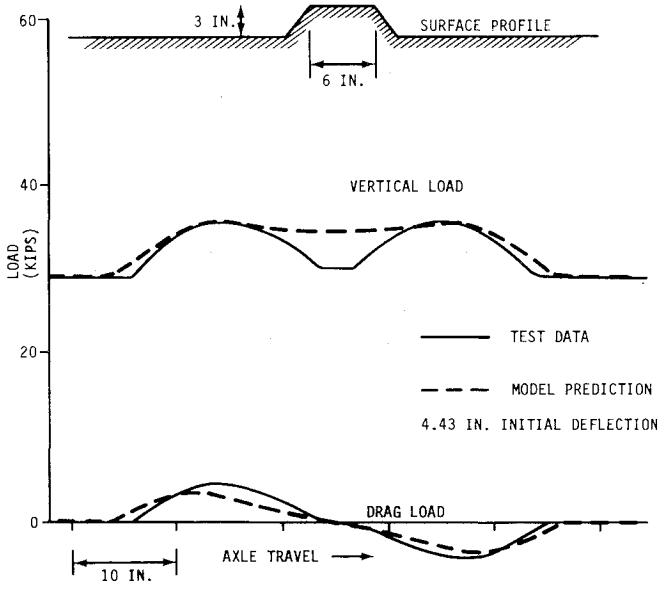

Fig. 14 Fixed axle excursion over 6 × 3-in. bump.

defined by $a\hat{u}_1\hat{u}_2$ is

$$F_b = C_b \int_{\hat{u}_1}^{\hat{u}_2} [(mu+b) + (R_b^2 - u^2)^{1/2}]\,du \tag{26}$$

where C_b is the product of the contact area width and the elastic modulus of the tire carcass, and

$$R_b = R_0 - B_t \tag{27}$$

The boundaries $\hat{u}_1$ and $\hat{u}_2$ for the bottomed tire section (like $\hat{u}_1$ and $\hat{u}_2$) are defined by the endpoints of each surface element (such as $\hat{u}_2$) and/or the intersection of the tire bottoming threshold B_t and the surface profile element (such as $\hat{u}_1$). Thus, integrating Eq. (26) yields

$$F_b = \tfrac{1}{2}C_b[m(\hat{u}_2^2 - \hat{u}_1^2) + 2b(\hat{u}_2 + \hat{u}_1) + \hat{u}_2(R_b^2 - \hat{u}_2^2)^{1/2} - \hat{u}_1(R_b^2 - \hat{u}_1^2)^{1/2} + R_b^2(\sin^{-1}\hat{u}_2/R_b - \sin^{-1}\hat{u}_1/R_b)] \tag{28}$$

In addition, it is assumed that the bottoming load acts on a line passing through the wheel axle and the midpoint of the surface profile between $\hat{u}_1$ and $\hat{u}_2$. Therefore

$$F_{buk} = -F_b v_m / R_m \tag{29a}$$

$$F_{buk} = F_b u_m / R_m \tag{29b}$$

where

$$u_m = \tfrac{1}{2}(\hat{u}_1 + \hat{u}_2) \tag{29c}$$

$$v_m = mu_m + b \tag{29d}$$

$$R_m = (u_m^2 + V_m^2)^{1/2} \tag{29e}$$

Input Parameters

Seven tire parameters are required to predict loads for a specific tire, in addition to the surface profile definition $(x_1,z_1),\ldots,(x_n,z_n)$. Six of these parameters are directly available from the tire manufacturer's load-deflection data sheet. They are R_0, P_0, B_t, L_t, B_b, and L_b. The seventh parameter, P_c, is obtained from the tire load data replotted as a function of P_0 for a family of constant δ curves, as shown in Fig. 9.

Four tire model constants, C_V, W_t, R_b, and C_b are evaluated using these seven parameters. The tire volume constant C_V is evaluated from Eq. (21). The effective tire section width W_t is evaluated from Eqs. (1), (11), (19), and (22) for $\delta = B_t$, $F_v = L_t$, and $F_{bv} = 0$. Thus

$$W_t = \frac{L_t}{P_{\delta=B_t}(A_v/W_t)_{\delta=B_t}}$$

The bottoming threshold radius R_b is determined from Eq. (27).

Following the evaluation of C_V and W_t, the pneumatic equations are used to evaluate the tire bottoming constant C_b. Solving Eqs. (11), (17), (22), and (28) for $\delta = B_b$, and then substituting into Eq. (1) yields

$$C_b = \frac{L_b - (PA_v)_{\delta=B_b}}{(F_b/C_b)_{\delta=B_b}}$$

Computer Program

A computer subprogram has been developed by the author, based on the tire model equations presented, that achieves the stated objective of computational efficiency compatible with digital aircraft taxi simulations. The subprogram is called

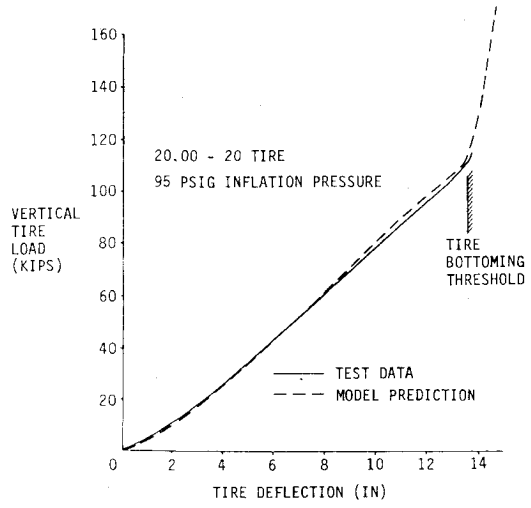

Fig. 15 Tire vertical load vs deflection.

once during the evaluation of the state equations for each tire in the simulation. The tire model equations are explicitly solved requiring no iteration.

The computational procedure begins by determining the limits $\bar{u}_1$ and $\bar{u}_2$ for each tire section ($k=1,2,\ldots$) based on the given position of the wheel axle x_s and z_s in relation to the surface profile. For each section Eqs. (4), (6), (9), (11), and (17) are evaluated to determine A_{vk}, A_{uk}, and V_k'/V_t. If the surface profile penetrates the area defined by R_b, tire bottoming loads F_{vk} and F_{uk} are calculated using Eqs. (28) and (29a-29e). Following the evaluation of tire properties for each section, the effective pneumatic pressure is determined from Eqs. (3c) and (22). Finally the total vertical and drag loads F_v and F_u are calculated using Eqs. (1), (2), (3a), (3b), (3d), and (3e). Logical paths are provided for cases where a simpler set of equations can be used, such as when no tire contact is made with the surface profile or when the total tire footprint is on a flat portion of the surface profile.

Model Verification

Model predictions are compared with tire test data in Figs. 12-14. The test data are taken from a C-130 main gear tire (20.00-20) traversing rectangular bumps and dips at a speed of 3-in./s for fixed axle heights. The data were generated on the Flat Surface Tire Force Machine at the Mechanical Branch of the Flight Dynamics Laboratory (FDL) at Wright-Patterson Air Force Base (WPAFB). The machine measures the resulting vertical and drag loads at the wheel axle.

The input data for the pneumatic tire model used to generate the load predictions are $R_0=27.5$ in.; $P_0=95$ psi; $P_c=21$ psi; $B_t=13.4$ in., $L_t=110{,}000$ lb; $B_b=14.0$ in., $L_b=130{,}000$ lb.

The comparison of tire excursion test data and model predictions indicates good quantitative correlation for both vertical and drag loads. In Fig. 15 model predictions for tire load vs tire deflection against a flat surface are compared with test data taken from a B.F. Goodrich tire data sheet. The model predictions correlate closely with test data and illustrate the tire bottoming load capability of the tire model.

Computational Efficiency

The operating speed of an aircraft taxi simulation using the pneumatic tire model was compared with the same aircraft simulation using a point contact spring tire model in a series of bench mark tests to assess their relative computational efficiency.

The spring model is a four-part piecewise linear representation of the tire load-deflection curve, and is evaluated in the simulation with a table lookup routine. The aircraft simulation represents a 400,000-lb gross weight transport with 14 main and nose gear wheels. The simulation has 28 state equations that describe rigid body and elastic airframe freedoms. The integration process utilizes a fourth-order, variable time step Runge-Kutta algorithm.

Constant speed aircraft excursions at 60 knots were simulated over three surface profiles. They were 1) a 4-ft × 3-in. ramp, 2) a pair of 2-ft × 2.5-in. deep surface spalls, and 3) a series of six 2-ft × 2-in. spalls. Each simulation generated 2 s of time-history, which was sufficient to assess the aircraft dynamic response.

For each bench mark test defined above the consumption of central processor time for the aircraft simulation with the pneumatic tire model was within 1% of that required for the same simulation with the spring tire model. Thus, even though the number of equations in the pneumatic tire model is much greater than those for the spring tire model, the increase in size of the total aircraft simulation equation set is insignificant.

Conclusions

The pneumatic tire model accurately predicts tire vertical and drag loads induced by surface irregularities, including bumps shorter than the tire footprint length. Based on comparisons with tire test data it can be concluded that the tire model duplicates the enveloping characteristics of a pneumatic tire. However, verification has only been achieved for low-speed tire excursions. The significance of high rolling speed in terms of the contribution of carcass dynamics (or other phenomena) to the net tire loads is not known.

Bench mark comparisons of the pneumatic tire model and a simple spring tire model demonstrate that the pneumatic tire model is a computationally efficient algorithm suitable for aircraft digital taxi simulation.

Acknowledgments

This work was conducted under an IR&D project funded by the Boeing Military Airplane Company. The author is indebted to the Mechanical Branch of the FDL, WPAFB, for the tire test data used in the model verification.

References

[1] Wignot, J.E., Durup, P.C., Gamon, M.A., Ginsburg, T.A., and Ortasse, R., "The Development of Dynamic Taxi Design Procedures," FAA DS-68-11, June 1968, p. D-25.

[2] Schuring, D. and Belsdorf, M.R., "Analysis and Simulation of Dynamical Vehicle—Terrain Interaction," Cornell Aeronautical Laboratory, Inc., Buffalo, N.Y., CAL Tech. Memo. VJ-2330-G-56, May 1969.

[3] Clark, S.K., "The Rolling Tire Under Load," SAE Paper 650493, May 1965.

[4] Lippmann, S.A. and Nanny, J.D., "A Quantitative Analysis of the Enveloping Forces of Passenger Tires," SAE Paper 670174, Jan. 1967.

[5] Smiley, R.F. and Horne, W.B., "Mechanical Properties of Pneumatic Tires With Special Reference to Modern Aircraft Tires," NASA Tech. Rept. R-64, 1957, p. 7.